scientific data

OPEN

DATA DESCRIPTOR

Reconstruction of all-sky daily air temperature datasets with high accuracy in China from 2003 to 2022

Min Wang[1,2], Jing Wei[3], Xiaodong Wang[4], Qingzu Luan[5] ✉ & Xinliang Xu[1,2]

A high-accuracy, continuous air temperature (Ta) dataset with high spatiotemporal resolution is essential for human health, disease prediction, and energy management. Existing datasets consider factors such as elevation, latitude, and surface temperature but insufficiently address meteorological and spatiotemporal factors, affecting accuracy. Additionally, no high-resolution dataset currently includes daily maximum (T_{max}), minimum (T_{min}), and mean (T_{mean}) temperatures generated using a unified methodology. Here, we introduce the four-dimensional spatiotemporal deep forest (4D-STDF) model, integrating 12 multisource factors, encompassing static and dynamic parameters, and six refined spatiotemporal factors to produce Ta datasets. This approach generates three high-accuracy Ta datasets at 1 km spatial resolution covering mainland China from 2003 to 2022. These datasets, in GeoTIFF format with WGS84 projection, comprise daily T_{max}, T_{min}, and T_{mean}. The overall RMSE are 1.49 °C, 1.53 °C, and 1.18 °C for the estimates. The 4D-STDF model can also be applied to other regions with sparse meteorological stations.

Background & Summary

In global warming, generating high-resolution Ta datasets is becoming increasingly important. High-precision, high spatiotemporal resolution, and long-term continuous temperature datasets, particularly those capturing extreme temperatures, are essential for understanding small-scale climate changes[1], such as urban heat islands and mountain microclimates; identifying seasonal temperature characteristics and abnormal weather events[2,3]; enhancing building energy efficiency[4]; predicting and controlling diseases[5–7]; and improving human health research[8,9]. Despite the accurate observation, capture, and recording of spatiotemporal variations in Ta surround stations by widely distributed meteorological stations, they fall short of providing a detailed depiction of Ta's spatiotemporal distribution and variation patterns for the whole area. There are already a lot of gridded Ta datasets to fill this gap (Table 1). From the Table 1, we find that existing Ta datasets primarily serve large-scale climate assessments and have relatively low spatiotemporal resolution[10–15] (e.g., monthly or 8-day intervals, 0.1° or 0.05°). While some datasets have achieved daily 1 km spatial resolution, their periods are short (only a particular year or before 2020), or they estimate only one or two of the T_{max}, T_{min}, or T_{mean} temperatures, and their estimation accuracy (e.g., for extreme temperature T_{max} and T_{min}, the highest accuracy is reported by Zhang *et al.* with RMSE above 1.5 °C) still has room for improvement[16–19].

Three approaches can be used to estimate gridded Ta products: the temperature vegetation index (TVX) assumption model, physical-mechanical models, and statistical models. However, the TVX assumption model exhibits significant estimation errors in areas with low vegetation cover[20]. In contrast, physical models require high parameter inputs[21], making them computationally intensive and difficult to implement on a large scale. Furthermore, methods relying on atmospheric profiles become ineffective when the inversion layer appears[22,23]. Statistical models, such as Spatiotemporal Regression-Kriging[16], Geographic Weighted Regression model[24], Bayesian Kriging Regression Method[25], and Spatially Varying Coefficient Models with Sign Preservation (SVCM-SP)[17], known for their simplicity and high accuracy, have gained widespread application. Although

[1]State Key Laboratory of Resources and Environmental Information System, Institute of Geographic Sciences and Natural Resources Research, Chinese Academy of Sciences, Beijing, 100101, China. [2]University of Chinese Academy of Sciences, Beijing, 100049, China. [3]Department of Atmospheric and Oceanic Science, Earth System Science Interdisciplinary Center, University of Maryland, College Park, Maryland, 20742, USA. [4]Beijing Visiorld Technology Co., Ltd, 100029, Beijing, China. [5]Beijing Municipal Climate Center, Beijing Meteorological Bureau, Beijing, 100089, China. ✉e-mail: qzluan@gmail.com

	Literature	Spatial extent	Spatial resolution	Temporal frequency	Coverage time	Accuracy		
						MAE	RMSE	R^2
1	(Hooker *et al.*)[11]	Global	0.05°	Monthly (T_{mean})	2003–2016	—	1.14–1.55 °C	—
2	(Funk *et al.*)[12]	Global	0.05°	Monthly (T_{max})	1983–2016	0.8–1.0 °C	—	0.61–0.85
3	(Yao *et al.*)[13]	Global	30 arcsecond	Monthly (T_{max}, T_{min}, and T_{mean})	2001–2020	Validated using CMIC: T_{max}: 1.373 °C T_{min}: 1.105 °C T_{mean}: 0.770 °C	Validated using CMIC: T_{max}: 2.223 °C T_{min}: 1.516 °C T_{avg}: 1.056 °C	Validated using CMIC: T_{max}: 0.959 T_{min}: 0.984 T_{avg}: 0.991
4	(Chen *et al.*)[10]	China	1 km	8-day (T_{max}, T_{min}, and T_{mean})	2010	—	T_{max}: 1.45 °C T_{min}: 1.29 °C T_{avg}: 1.2 °C	0.93–0.99
5	(Fang *et al.*)[14]	China	0.1°	Daily (T_{max}, T_{min}, and T_{mean})	1979–2018	T_{max}: 0.63–1.40 °C T_{min}: 0.58–1.60 °C T_{mean}:0.27–0.68 °C	T_{max}: 0.86–1.78 °C T_{min}: 0.78–2.09 °C T_{mean}:0.35–1.00 °C	T_{max}: 0.96–0.99 T_{min}: 0.95–0.99 T_{mean}:0.99–1.00
6	(P. Wang *et al.*)[15]	China	0.1°	Daily (T_{max})	1979–2018	1.07 °C	1.52 °C	—
7	(Chen *et al.*)[18]	Mainland China	1 km	Daily (T_{mean})	2003–2019	1.033K–1.100 K	1.342K–1.440 K	0.984–0.986
8	(Kilibarda *et al.*)[16]	Global	1 km	Daily (T_{max}, T_{min}, and T_{mean})	2011	—	T_{max}: 2.6 °C T_{min}: 2.7 °C T_{avg}: 2.4 °C	T_{max}: 0.96 T_{min}: 0.94 T_{avg}: 0.97
9	(Zhang *et al.*)[17]	Mainland China	1 km	Daily (T_{max} and T_{min})	2003–2016	T_{max}: 1.22 °C T_{min}: 1.30 °C	T_{max}: 1.75 °C T_{min}: 1.82 °C	T_{max}: 0.93 T_{min}: 0.94
10	(Zhang *et al.*)[19]	Global	1 km	Daily (T_{max} and T_{min})	2003–2020	Europe and Asia: T_{max}: 1.29 ± 0.15 °C T_{min}: 1.28 ± 0.20 °C	Europe and Asia: T_{max}: 1.80 ± 0.19 °C T_{min}: 1.75 ± 0.26 °C	—

Table 1. The ten mainly existing gridded Ta datasets.

statistical models consider the spatiotemporal heterogeneity of Ta and incorporate some influencing factors, they often struggle to integrate all aspects, such as climatic conditions, human activities, and topography, due to their computational complexity and efficiency issues. This limitation makes it challenging to accurately capture Ta variations over time and space, particularly for extreme temperatures (T_{max} and T_{min}). For instance, while the Spatiotemporal Regression-Kriging model integrates spatial and temporal data correlations and offers rich spatiotemporal prediction capabilities, its RMSE is around 6 °C in areas with sparse weather stations or at altitudes above 1000 m, making accurate prediction a challenge[16]. The GWR method handles spatial non-stationarity and establishes local relationships but performs better in warm seasons and flat areas and is less accurate than Kriging in cold seasons[24]. The Bayesian Kriging Regression Method incorporates Kriging regression within a Bayesian framework to account for uncertainties in the estimation process but relies solely on LST data without considering other influencing factors[25]. The SVCM-SP model, which introduces signed spatially varying coefficients, addresses the anomalies in GWR's relationship between Ta and explanatory variables, offering improved accuracy. However, it uses only LST and DEM parameters, neglecting other factors such as clouds, snow, land cover types, and meteorological parameters, leading to discrepancies between the estimated and actual Ta spatial patterns[17].

Machine learning (ML) methods have demonstrated superior data mining capabilities compared to traditional regression models. Their high computational efficiency[26,27] and significant enhancement of estimation accuracy[28,29] make ML models, such as Rule-based Cubist Regression[30], Cubist Matching Learning Algorithm[31], Random Forest[32–34], Spatiotemporal Random Forest[35], and fusion of various statistical models[36], widely applicable in Ta estimation. ML models notably improve Ta estimation accuracy compared to statistical regression methods[28,29]. However, most current Ta estimation models simplistically adopt ML techniques, often neglecting the spatiotemporal heterogeneity of Ta. This neglect leads to significant errors, especially in areas with complex terrain or sparse monitoring stations. To address this issue, integrating spatiotemporal information with ML models is becoming an essential trend. For example, Sun *et al.*[37] integrated deep learning models with spatial statistical information for estimating urban and rural surface ozone products from 1990 to 2019. Similarly, Wei *et al.* successfully fused spatiotemporal information with artificial models for estimating $PM_{2.5}$[38–40], NO_2[41], PM_1[42], and $PM_{2.5}$ chemical composition[43]. These studies highlight the advantages of incorporating spatiotemporal information to improve model performance by extrapolating station observation data to the surface. However, its application in Ta estimation models has been relatively limited.

Although ML models have significantly improved Ta estimation accuracy, the precision of these models is highly dependent on the proper selection of parameters. Incorrect or suboptimal parameter choices can still lead to significant errors, especially in areas with complex terrain or sparse monitoring stations[26]. Based on existing research, there is high consistency in the selection of variables when establishing the relationship between observed Ta at stations and auxiliary variables. Primary considerations include static parameters such as geographical factors (longitude, latitude, and elevation) and temporal parameters[10,24,44]. However, static parameters alone cannot capture the influence of biophysical factors such as land cover, vegetation characteristics, and human activities. Subsequently, dynamic parameters such as Land Surface Temperature (LST), Normalized Difference Vegetation Index (NDVI), Downward Shortwave Radiation (DSR), Surface Albedo (ALB), and Leaf Area Index (LAI) have been added to the model to enhance further its ability to depict details of Ta[28,45,46]. Although selecting these parameters considers the impact of topography and human activities,

meteorological factors such as evapotranspiration, wind speed, precipitation, and atmospheric pressure, which are equally crucial to Ta, are usually neglected in model incorporation[33,34]. Moreover, incorporating spatiotemporal information in ML models has yielded superior estimations of various air pollution indicators, such as ozone[37], $PM_{2.5}$[38–40], NO_2[41], PM_1[42], and $PM_{2.5}$ chemical composition[43]. In this study, we pay particular attention to meteorological factors and spatiotemporal information in model training and inversion to improve Ta estimation accuracy.

Numerous studies have indicated that LST improves estimation accuracy and captures spatiotemporal variations of Ta in detail, making it a key parameter in the inversion process of Ta products. However, due to data gaps caused by factors such as clouds, LST data may not fully support the production of continuous spatiotemporal temperature products. Currently, there are generally two strategies to address this issue. The first strategy involves estimating Ta based on available LST data and then using various interpolation and reconstruction methods to complete Ta. The second strategy consists of producing fully covered LST products for the inversion of Ta. Previous research has shown that models estimating surface temperature with gap-filling perform better overall, demonstrating satisfactory accuracy and the ability to overcome issues related to cloud contamination[30]. Therefore, this study adopts the second strategy, selecting high-precision, full-coverage LST products as training parameters for all-sky daily continuous Ta estimation.

Based on previous research, our study adopts the 4D-STDF model, which considers the inherent characteristics of Ta and comprehensively accounts for spatial differences, seasonality, and diurnal variations to estimate high-quality daily T_{max}, T_{min}, and T_{mean} products over a long time series. To our knowledge, this is the first reconstruction of all-sky daily T_{max}, T_{min}, and T_{mean} datasets at a 1 km resolution (2003–2022) in China. These datasets effectively support applications such as extreme climate monitoring, urban thermal environment ecological assessments, and energy consumption evaluations at small scales.

Methods

The workflow developed for reconstructing daily T_{max}, $T_{min,}$ and T_{mean} datasets based on the 4D-STDF model using multisource data is depicted in Fig. 1. The approach consists of three main steps. First, we pre-process multisource data, perform spatiotemporal matching and calculate spatiotemporal factors. Second, we train and adjust the estimation models for daily T_{max}, $T_{min,}$ and T_{mean} using the 4D-STDF model on an annual basis. Finally, we evaluate the model's performance through 10-fold cross-validation spanning the years 2003 to 2022.

Data sources and processing. We obtained point measurements of near-surface air temperature (NSAT) and spatially continuous variables (Table 2) used in NSAT estimation models from publicly available datasets outlined in Fig. 2.

Ground-based air temperature. The ground-based temperature data could obtain from the Chinese National Meteorological Information Center (http://data.cma.cn/) of the China Meteorological Administration (CMA), including 2,461 ground sites across mainland China, covering the period from 2003 to 2022 (Fig. 2). These datasets, including daily T_{max}, $T_{min,}$ and T_{mean} temperatures, were used to build the Ta estimation models and assess the performance of the models. Before dataset publication, rigorous quality control procedures were applied to ensure data integrity. However, to further ensure data quality, we excluded overflow values, identified and removed outliers, and handled missing values. Additionally, a thorough verification of the spatiotemporal consistency of the station data was performed, retaining meteorological stations with long monitoring durations and stable temperature values.

Seamless daily LST. The global seamless daily LST dataset from 2003 to 2022 was acquired from Iowa State University's DataShare (https://doi.org/10.25380/iastate.c.5078492) with a resolution of 1 km in the ellipse sinusoidal projection[47]. The dataset contains daytime and nighttime LST data in GeoTIFF format, with a unit of 0.1 degrees Celsius (°C), and has higher accuracies with RMSEs of 1.88 and 1.33 °C, respectively[48]. The seamless daily LST data for mainland China were selected, and the daily average LST was calculated from day and night data, which were used as the primary input variables for building the Ta estimation models.

Auxiliary data. The auxiliary data used in this study include meteorological, radiational, land use, topographic, and population data. The meteorological variables were sourced from the ERA5-Land hourly data (available from 1950 to the present) provided by Copernicus Climate Data Store (https://cds.climate.copernicus.eu/cdsapp#!/dataset/reanalysis-era5-land?tab=overview). These variables include boundary layer height (BLH), evaporation (ET), total precipitation (PRE), relative humidity (RH), surface pressure (SP), wind speed (WS), and wind direction (WD). All hourly data were aggregated into daily data to align with the daily seamless LST data. The radiational were obtained from the MODIS MCD18A1 products, accessible through NASA's Earth Observing System Data and Information System (EOSDIS) (https://search.earthdata.nasa.gov/search?q=MCD18A1). Land use data were derived from the MODIS MOD13A3 normalized difference vegetation index (NDVI) product, also available through EOSDIS (https://search.earthdata.nasa.gov/search?q=MOD13A3). Topographical data were acquired from the Shuttle Radar Topography Mission (SRTM) datasets provided by the CGIAR Consortium for Spatial Information (CGIAR-CSI) (http://srtm.csi.cgiar.org/). Population data were sourced from the Monthly Cloud-free DNB Composite datasets provided by Earth Observation Group (EOG) (https://eogdata.mines.edu/products/vnl/). All variables were resampled to a spatial resolution of 1 km × 1 km using the bilinear interpolation method. This resampling was conducted to ensure consistency with maximum, minimum, and mean temperatures recorded at each station.

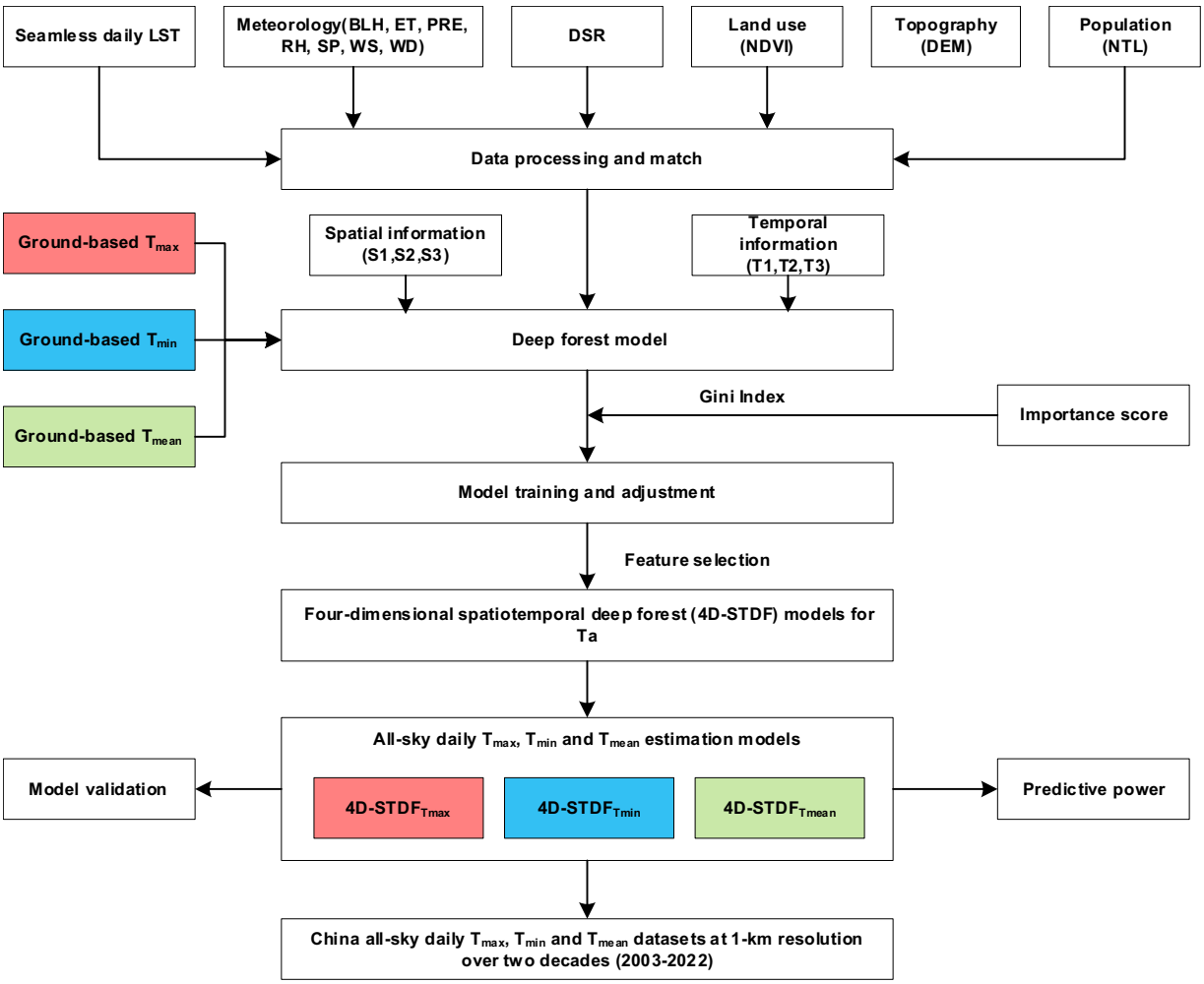

Fig. 1 The workflow for constructing and validating daily Ta (T_{max}, $T_{min,}$ and T_{mean}) datasets.

Dataset	Variable	Content	Unit	Spatial resolution	Temporal resolution	Data source
Surface air temperature	T_{max}	daily maximum temperatures	°C	*in situ*	Daily	Chinese National Meteorological Information Center
	T_{min}	daily minimum temperatures				
	T_{mean}	daily mean temperatures				
Seamless daily LST	LST	Daytime LST	°C	1 km × 1 km	Daily	Iowa State University's DataShare
		Nighttime LST				
Meteorology	BLH	Boundary layer height	m	0.1° × 0.1°	1 h	ERA5
	ET	Evaporation	mm		1 h	
	PRE	Total precipitation	mm		1 h	
	RH	Relative humidity	%		1 h	
	SP	Surface pressure	hPa		1 h	
	WS	10 m wind speed	Ms^{-1}		1 h	
	WD	10 m wind direction	degree		1 h	
DSR	DSR	Downward Shortwave Radiation	Wm^{-2}	1 km × 1 km	Daily	MCD18A1
Land use	NDVI	NDVI	—	1 km × 1 km	Monthly	MOD13A3
Topography	DEM	DEM	m	90 m × 90 m	—	SRTM
Population	NTL	Nighttime lights	$W\ cm^{-2}\ sr^{-1}$	500 m × 500 m	Monthly	VIIRS

Table 2. Input data sources used in this study.

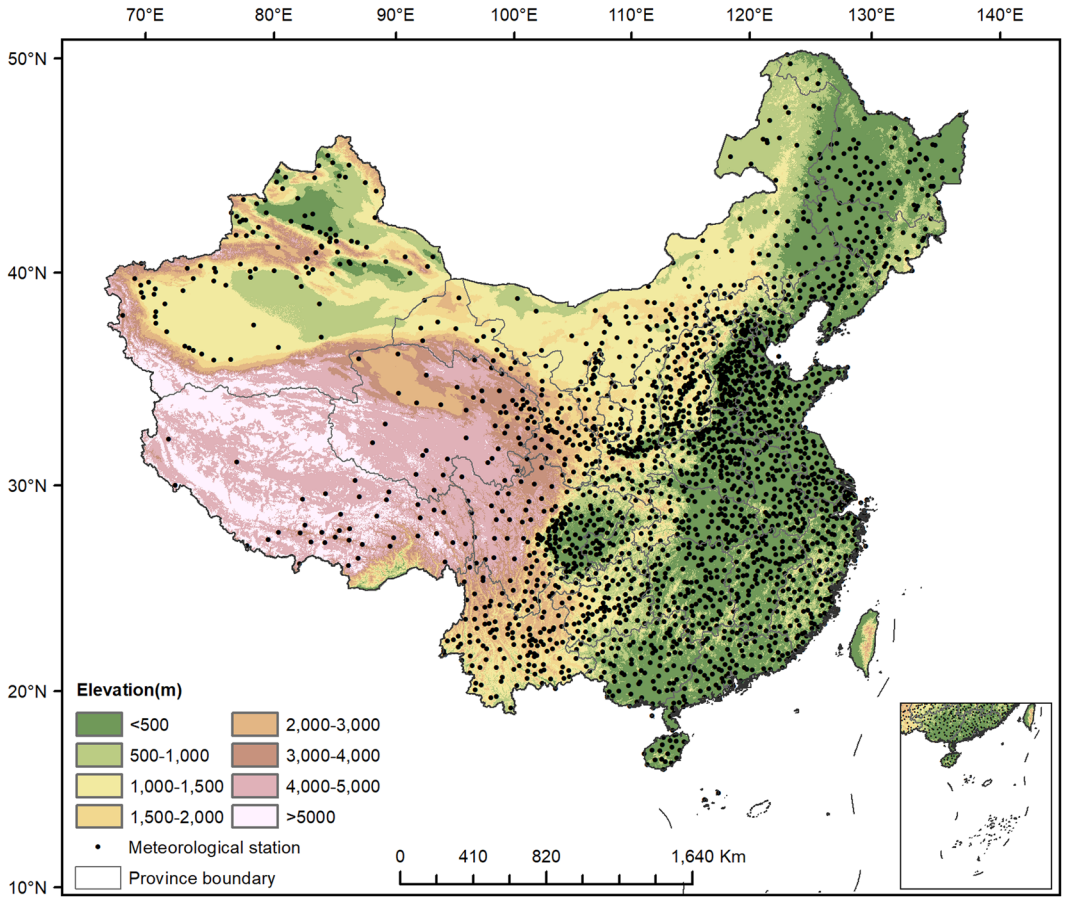

Fig. 2 The distribution of 2461 meteorological stations on the elevation map of China.

All-sky daily T_{max}, T_{min} and T_{mean} estimation models. After rigorous quality control, the number of samples used for model training each year exceeds 800,000, constituting a large dataset for model training. Therefore, the deep forest model is chosen to construct all-sky daily T_{max}, T_{min}, and T_{mean} estimation models. Compared to traditional decision trees and random forest, the deep forest model demonstrates higher randomness, greater computational efficiency, and stronger generalization ability, especially in cases of large datasets with high dimensionality or the need for higher computational efficiency[49]. The trained predictive model exhibits greater robustness and a reduced risk of overfitting, making it more suitable for training and predicting Ta.

In this study, the seamless daily T_{max}, T_{min} and T_{mean} should be estimated, so the ground-based Ta of max, min and mean are considered true values, respectively. The seamless daily average LST is used as the primary input for the 4D-STDF model, along with all auxiliary factors, including meteorological variables (BLH, ET, PRE, RH, SP, WS and WD), DSR, NDVI, DEM, NTL, and spatiotemporal variables (S1, S2, S3, T1, T2 and T3) for training. Three spherical coordinates (S1, S2, S3) are used to express the spatial variables, and three helix-shape trigonometric vectors (T1, T2, T3) are used to express the seasonal cycles and daily variations[43] for daily T_{max}, T_{min} and T_{mean}:

$$Ps = [S1, S2, S3] = \left[\cos\left(2\pi\frac{Lon}{360}\right)\cos\left(2\pi\frac{Lat}{180}\right), \cos\left(2\pi\frac{Lon}{360}\right)\sin\left(2\pi\frac{Lat}{180}\right), \sin\left(2\pi\frac{Lon}{360}\right)\right] \quad (1)$$

$$Pt = [T1, T2, T3] = \left[\frac{\mathrm{DOY}}{N}, \cos\left(2\pi\frac{DOY}{N}\right), \sin\left(2\pi\frac{DOY}{N}\right)\right] \quad (2)$$

During model training, the selection of feature importance is determined through the calculation of the Gini coefficient. It is essential to note that this result solely reflects the importance of variables in the 4D-$STDF_{Tmax}$, 4D-$STDF_{Tmin}$, 4D-$STDF_{Tmean}$ model training processes, rather than presenting the actual mechanistic contribution rate[50]. The results (Supplementary Fig. S1) indicate that, for the 4D-$STDF_{Tmax}$, 4D-$STDF_{Tmin}$, 4D-$STDF_{Tmean}$ models, LST is the most crucial indicator, with the largest importance scores of approximately 50%, 45%, and 50%, respectively. Following closely is the temporal factor T2, exhibiting importance scores exceeding 25% in all cases. The meteorological factor ET and the spatial factor S1 also play substantial roles, contributing approximately 10% and greater than 2%, respectively. The NDVI factor representing land use data, holds an importance

Dataset name	Links	Description
Daily T_{max}	https://doi.org/10.5281/zenodo.10983219	Daily T_{max} from the years 2003–2012
	https://doi.org/10.5281/zenodo.10983207	Daily T_{max} from the years 2013–2022
Daily T_{min}	https://doi.org/10.5281/zenodo.10951765	Daily T_{min} from the years 2003–2012
	https://doi.org/10.5281/zenodo.10983199	Daily T_{min} from the years 2013–2022
Daily T_{mean}	https://doi.org/10.5281/zenodo.10947354	Daily T_{mean} from the years 2003–2012
	https://doi.org/10.5281/zenodo.10983177	Daily T_{mean} from the years 2013–2022

Table 3. The datasets links in Zenodo.

of around 2%, underscoring its significance. The remaining 13 factors exhibit importance scores below 2%, indicating their lesser significance in the model. Of particular note is the significantly higher importance of the spatial factor S1 in 4D-STDF$_{Tmin}$ compared to the other two models, indicating the crucial role of spatial heterogeneity in estimating T_{min}. Throughout the construction and training of 4D-STDF models, parameters were judiciously selected based on the importance of factors to ensure the development of robust models.

Assessment of dataset accuracy and effectiveness. Ten-fold cross-validation (10-CV) is commonly used to validate the accuracy of Ta datasets[13,17,18,51]. In this study, we adopt two different cross-validation approaches at sample and spatial scales: sample-based 10-CV and spatial-based 10-CV.

The sample-based 10-CV randomly selects samples for validation, ensuring balanced use of all stations and seasons, making it ideal for overall performance evaluation. In this approach, all samples are randomly divided into 10 equal subsets. The model is trained using data from 9 of these subsets, while data from the remaining subset are used for independent validation. This process is repeated 10 times, and the final evaluation is based on the average of all validation results. The spatial-based 10-CV, also known as the out-of-station approach, is a spatially independent validation method that accounts for the spatial distribution of monitoring stations. In this approach, all monitoring stations in China are randomly divided into 10 equal subsets. The model is trained using data from 9 of these subsets (90% of the stations), while data from the remaining subset (10% of the stations) are used for independent validation. This method is commonly employed to assess a model's spatial predictive ability in areas without ground measurements across the entire country in most previous ML studies[52,53].

The accuracy of the model is quantitatively assessed using a linear regression equation, and the coefficient of determination (R^2) and model uncertainty are evaluated through root mean square error (RMSE) and mean absolute error (MAE). The annual evaluation accuracy was calculated based on the sample-based CV results for all stations. Similarly, for each station, evaluation parameters could be calculated based on the accuracy of the time series estimation. For each day, the evaluation accuracy was calculated based on all the stations. This method provides a conservative estimate of data uncertainty since the final results used all available data.

Data Records

The all-sky daily T_{max}, T_{min}, and T_{mean} datasets covering mainland China are currently freely available on Zenodo. Links to these datasets for the period from 2003 to 2022 are provided in Table 3. The datasets consist of six components: daily T_{max} from the years 2003–2012[54], daily T_{max} from the years 2013–2022[55], daily T_{min} from the years 2003–2012[56], daily T_{min} from the years 2013–2022[57], daily T_{mean} from the years 2003–2012[58] and daily T_{mean} from the years 2013–2022[59]. All data are in GeoTIFF format with a WGS84 projection and the unit of measurement is 0.1 degrees Celsius (°C).

Technical Validation

Overall accuracy assessment. Figure 3 illustrates the comprehensive sample-based 10-CV results of all daily, monthly, and annual T_{max}, $T_{min,}$ and T_{mean} estimates from all observed stations across mainland China for all study years. Overall, the estimation results exhibit high accuracy, with most samples evenly distributed around the 1:1 line, showing good agreement with ground-based T_{max}, $T_{min,}$ and T_{mean} observations. The overall RMSE values are 1.49 °C, 1.53 °C, and 1.18 °C for daily estimates; 1.38 °C, 1.65 °C, and 0.52 °C for monthly estimates; and 1.28 °C, 1.83 °C, and 0.41 °C for annual estimates, respectively. Supplementary Table S1 also reveals the strong performance of the models in estimating daily T_{max}, $T_{min,}$ and T_{mean} with R^2 greater than 0.98. In addition, daily T_{mean} exhibits the highest accuracy with MAE ranging from 0.81 °C to 0.99 °C and RMSE ranging from 1.13 °C to 1.27 °C. The accuracy of T_{max} and T_{min} is comparable, with MAE both ranging from 1.03 °C to 1.12 °C, RMSE ranging from 1.43 °C to 1.57 °C for T_{max} and from 1.46 °C to 1.57 °C for T_{min}. Supplementary Fig. S2 shows the total validation results of the models with R^2 values greater than 0.98 and RMSE values are 1.61 °C, 1.70 °C, and 1.32 °C for daily estimates, which are very close to the sample-based 10-CV results, indicating the model's predictive capability in areas without ground measurements across the entire country. These results suggest that the predicted datasets are good quality and suitable for fine-scale studies.

Spatial distribution of the accuracy. The spatial distribution of the accuracy of Ta estimation is assessed for T_{max}, T_{min} and T_{mean} across mainland China (Fig. 4). The 4D-STDF methods applied in different regions demonstrate varying levels of precision, with higher accuracy observed in the eastern regions ($R^2 > 0.95$, MAE and RMSE < 1.5 °C) and lower accuracy in the western regions ($R^2 < 0.9$, MAE and RMSE > 1.5 °C). T_{mean} estimates exhibit relatively small variations across the entire spatial domain, with most sites in the eastern region achieving RMSE < 1 °C. However, there are sporadic instances of lower precision in the western region, where

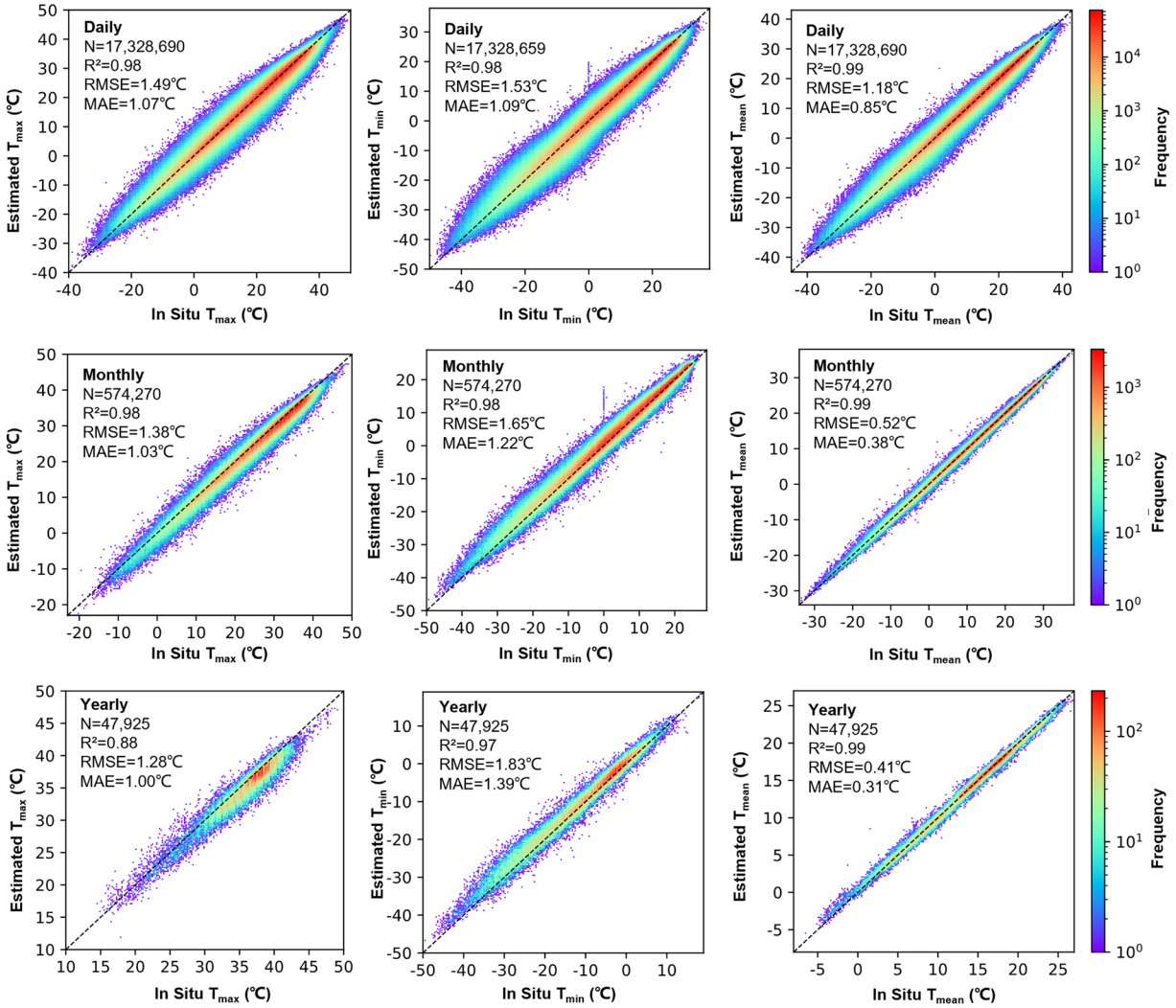

Fig. 3 Scatter diagrams illustrating the comprehensive sample-based 10-CV results for daily, monthly and annual estimates of T_{max}, T_{min} and T_{mean} from ground-based stations throughout the period from 2003 to 2022 in mainland China.

RMSE exceeds 2.0 °C; T_{max} estimates generally show higher accuracy in the south-eastern region, with RMSE predominantly below 1.5 °C, and in some isolated areas, estimation errors fall below 1.0 °C. Conversely, in the western and northern regions experience higher errors, with RMSE generally exceeding 2.0 °C and some sites surpassing 2.5 °C, particularly in the arid northwest; For T_{min}, the highest accuracy is observed in the central region of China, with errors generally below 1.0 °C. However, higher errors are concentrated in the cold areas of the northeast and northwest, where RMSE generally exceeds 2.5 °C. These spatial variations in Ta provide robust evidence for the reliability of our Ta datasets.

Seasonal distribution of the accuracy. We also evaluate the model performance at different seasons. The daily RMSE values of T_{max}, $T_{min,}$ and T_{mean} at the annual scale are presented in Fig. 5. The RMSE of T_{max}, $T_{min,}$ and T_{mean} show a clear seasonal variation, with peaks in winter and valleys in summer, indicating higher accuracy in summer and lower in winter. For T_{max}, the RMSE ranges from 1.3 °C to 1.7 °C, with a maximum seasonal difference of 0.4 °C, indicating relatively stable accuracy throughout the year. Compared to T_{max}, T_{min} exhibits a broader fluctuation range (1.0 °C to 2.0 °C), with a maximum seasonal difference of 1.0 °C, reflecting greater seasonal variability. The RMSE for T_{mean} is consistently lower than that for T_{max} and T_{min} throughout the year, consistent with prior research[13,44]. The RMSE for T_{mean} fluctuates between 0.9 °C and 1.5 °C, with a maximum seasonal difference of 0.6 °C, indicating that its accuracy shows a similar seasonal stability to T_{max}. Notably, during winter, the RMSE for T_{min} is around 1.8 °C, which is higher than the RMSE for T_{max} (around 1.5 °C), whereas in summer, the RMSE for T_{min} is around 1.2 °C, lower than that for T_{max} (around 1.4 °C). For T_{mean}, the estimation accuracy is not only higher than that for T_{max} and T_{min} throughout the year, but it also achieves the highest accuracy in summer, with RMSE dropping below 1 °C. These findings underscore the validity of the dataset in capturing seasonal variations and providing reliable Ta estimates, particularly for T_{max}, T_{min}, and T_{mean} during summer.

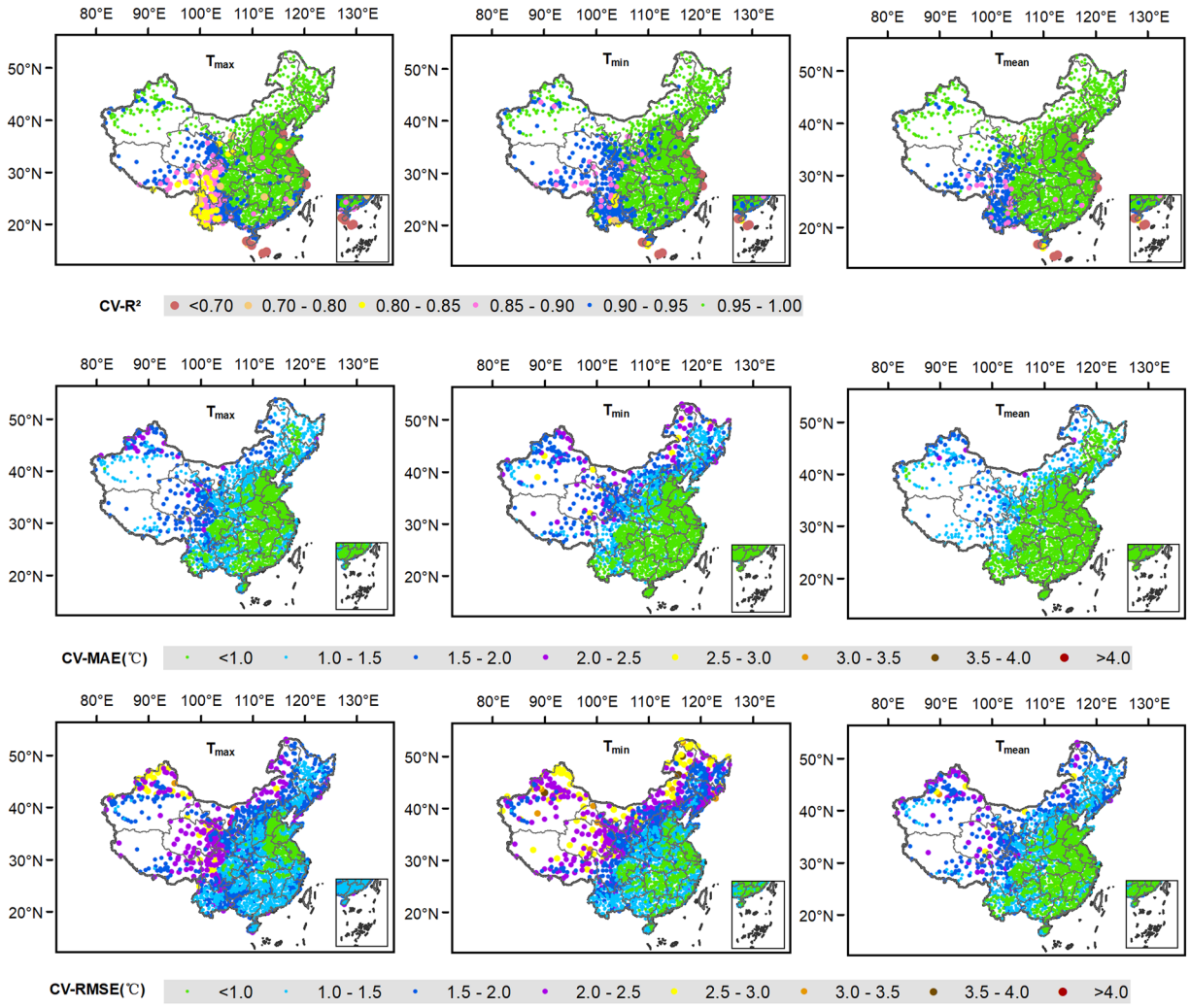

Fig. 4 Spatial patterns of R^2, MAE, and RMSE for T_{max}, T_{min}, and T_{mean} at stations of mainland China from 2003 to 2022.

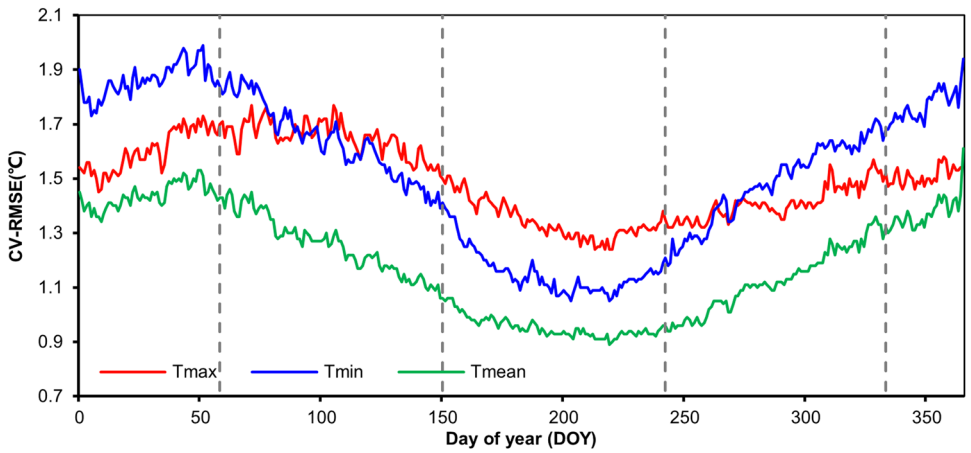

Fig. 5 Daily RMSE of T_{max} (red line), T_{min} (blue line), and T_{mean} (green line) across mainland China from 2003 to 2022.

Spatial variations of Ta datasets. The evaluations above indicate that our model demonstrates robust performance across multiple spatial and temporal scales. To illustrate the potential of our datasets, we examine

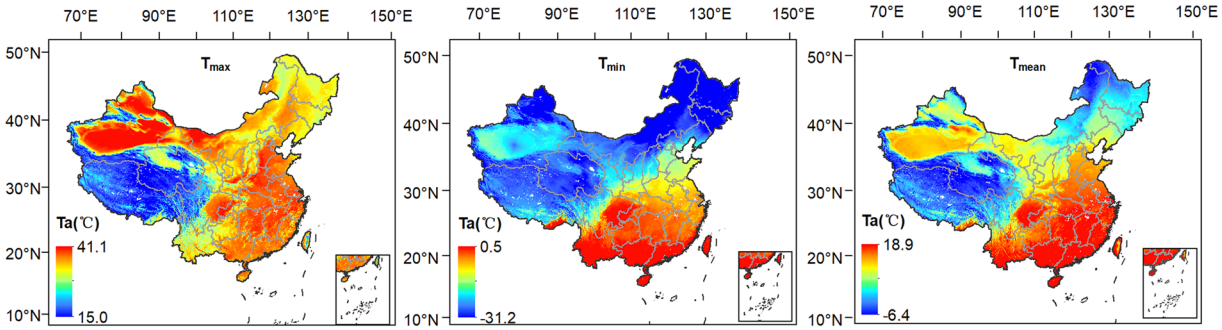

Fig. 6 Spatial pattern of average estimated Ta in mainland China from 2003 to 2022.

	T_{max}	T_{min}	T_{mean}
Daily			
MAE(°C)	1.07	1.09	0.85
RMSE(°C)	1.49	1.53	1.18
R^2	0.98	0.98	0.99
Monthly			
MAE(°C)	1.03	1.22	0.38
RMSE(°C)	1.38	1.65	0.52
R^2	0.98	0.98	0.99

Table 4. Accuracy of Ta datasets in this study.

the yearly changes of Ta and spatial variations averaged from 2003 to 2022 (Fig. 6). The lowest T_{max} values are observed in high-altitude regions, such as the Qinghai-Tibet Plateau, where temperatures hover around 15 °C. Conversely, lower latitudes tend to experience generally higher T_{max} values, with the maximum T_{max} occurring in arid and semi-arid regions at high latitudes, reaching an average T_{max} of approximately 41.1 °C. T_{min} values are lower in high latitudes, particularly in the northern areas and at high altitudes, reaching a minimum of −31.2 °C. As latitude decreases, T_{min} values tend to increase, with the highest reaching 0.5 °C. T_{mean} values are lowest in high latitudes and altitudes, gradually rising with decreasing latitude, with a maximum of 18.9 °C.

In summary, in arid and semi-arid regions at high latitudes, Ta is generally higher than in surrounding areas. The results indicate that the lack of vegetation and higher surface albedo lead to increased surface temperature, contributing to rise in Ta. These variations in Ta provide robust evidence for the reliability of our datasets.

Comparison with existing Ta datasets. Existing datasets typically have temporal resolutions focused on daily, monthly, or 8-day intervals, with spatial resolutions ranging from 30 arcseconds to 0.1° (Table 1). We compare our dataset's accuracy (Table 4) with the existing datasets in a comprehensive way.

The estimation of daily datasets. Fang *et al.*[14] achieved high precision in their temperature correction method, with RMSE ranging from 0.86 °C to 1.78 °C, 0.78 °C to 2.09 °C, and 0.35 °C to 1.00 °C. Still, their study's spatial resolution (0.1°) limited its ability to capture fine-scale temperature variations. Similarly, Wang *et al.*[15] estimated daily T_{max} with an accuracy similar to our study, yielding an MAE of 1.07 °C and an RMSE of 1.52 °C, yet their spatial resolution was also restricted to 0.1°. Kilibarda *et al.*[16] provided global daily T_{max}, T_{min}, and T_{mean} datasets but with lower accuracy, as their RMSE exceeded 2 °C. Chen *et al.*[18] estimated daily T_{mean} at a 1 km resolution in China, with a minimum RMSE of 1.342 °C, which is 0.162 °C higher than the RMSE in our study. Zhang *et al.*[17] reported RMSE averages of 1.75 °C for T_{max} and 1.82 °C for T_{min}, which are 0.26 °C and 0.29 °C higher, respectively, than our findings. When Zhang *et al.* [19] extended their study globally, their RMSE values for T_{max} and T_{min} were 1.80 ± 0.19 °C and 1.75 ± 0.26 °C, about 0.3 °C higher than those in our study.

The estimation of monthly datasets. Hooker *et al.*[11] produced a global monthly T_{mean} dataset for 2003–2016 at a 0.05° resolution, with RMSE values ranging from 1.14 °C to 1.55 °C, which are notably higher than our study's RMSE of 0.52 °C. Funk *et al.*[12] estimated a global 0.05° monthly T_{max} dataset, achieving an MAE of 0.8–1.0 °C, slightly better than our study's MAE of 1.03 °C, but with a lower spatial resolution. Yao *et al.*[13] estimated global monthly T_{max}, T_{min}, and T_{mean} at 30 arcseconds resolution from 2001 to 2020. Their results, with MAE and RMSE values of 1.373 °C, 1.105 °C, 0.770 °C and 2.223 °C, 1.516 °C, and 1.056 °C respectively, show lower accuracy for T_{max} and T_{mean} compared to our study, while the T_{min} estimates are comparable to ours. Chen *et al.*[10] achieved high precision for a 1 km Ta dataset in China for 2010, with RMSE values of 1.45 °C, 1.29 °C, and 1.2 °C for T_{max}, T_{min}, and T_{mean}, respectively. However, their study had a lower temporal resolution of 8 days, which limits direct comparison to our study's higher temporal resolution and accuracy.

Comparison of temporal and spatial accuracy for extreme temperature. Since the datasets conducted by Zhang *et al.*[17] and Zhang *et al.*[19] are consistent with this study's spatial and temporal resolution, a comparison of the accuracy from spatial and temporal in extreme temperature estimates was conducted. Figure 4 in Zhang *et al.*[17] shows that the RMSE for T_{max} estimated using the SVCM-SP method is predominantly between 1.0 and 1.5 °C, with few eastern stations having RMSE below 1.0 °C. In comparison, western regions with sparse stations often have RMSE above 1.5 °C, reaching up to 3.5 °C. Similarly, Fig. 4 in Zhang *et al.*[19] indicates T_{max} RMSE ranging from 1.0 to 2.0 °C in most parts of China, with the western plateau between 2.0 and 2.5 °C, and the northeast between 1.0 and 1.5 °C, with no regions below 1.0 °C. In contrast, this study significantly improves in T_{max} accuracy, with RMSE below 1.0 °C in North China and between 1.0 and 1.5 °C in South China and central regions. Even in sparsely monitored northwest areas, the maximum RMSE remains below 3.0 °C (Fig. 4). For T_{min}, although Zhang *et al.*[17] and Zhang *et al.*[19] show that regions with RMSE below 1 °C are mainly in the southeast, and sparsely monitored northwest areas have RMSE ranging from 2.0 to 4.0 °C, this study achieves reduced T_{min} RMSE across various regions, controlling values between 2.0 and 3.0 °C in sparsely monitored northwest and northeast areas. These results underscore the enhanced precision and broader applicability of the method used in this study across diverse geographic and climatic conditions.

In comparing the temporal distribution of RMSE, all three datasets exhibit a consistent seasonal variation trend, with higher accuracy in summer than in winter. In this study, the seasonal distribution of T_{max} RMSE ranges from 1.3 to 1.7 °C, and T_{min} from 1.0 to 2.0 °C, highlighting the high accuracy achieved (Fig. 5). In contrast, Fig. 5 from Zhang *et al.*[17] shows T_{max} RMSE between 1.5 to 2.0 °C and T_{min} from 1.5 to 3.0 °C. Similarly, Fig. 5 from Zhang *et al.*[19] shows that the temporal variation of RMSE for T_{max} and T_{min} across Asia ranges from 1 to 2.0 °C. This study demonstrates superior control over seasonal RMSE, achieving higher accuracy.

Although our datasets offer an approximately 0.3 °C improvement in the estimation of daily T_{max} and T_{min} compared to similar datasets, this enhancement is crucial given that a mere 0.5 °C increase in global temperatures can significantly amplify the occurrence of regional extreme heat events in China[60]. This 0.3 °C improvement in accuracy enables us to capture subtle temperature variations more precisely, leading to more reliable predictions of extreme events. Compared with the monitoring of heatwaves or extreme cold days based on weather stations or spatial interpolation data (e.g., Zhang *et al.*[61]; Liu *et al.*[62] and Ding and Qian[9]), this dataset provides a more detailed representation of the spatial distribution and trends of extreme weather events. Upon these analyses, our study's inverted dataset shows superior performance in terms of daily and monthly temporal scale, optimal spatial resolution (1 km), and maximum accuracy, especially for T_{max} and T_{min}.

Limitations and future work. Our study takes a more detailed approach by decomposing spatial and temporal coordinates to better capture their influence on the Ta estimation model. By incorporating 18 factors, using a deep forest model, and selecting optimal parameters based on spatiotemporal locations, we achieve greater accuracy, making these datasets and their estimation method valuable addition to existing temperature estimation products.

However, we should also notice that, despite achieving satisfactory accuracy when estimating daily, monthly, or annual Ta (Fig. 3), there may be instances of underestimating T_{max} or overestimating T_{min}. Specifically, results for T_{max} and T_{min} may skew rightward or leftward of the 1:1 line, respectively. This phenomenon can be attributed to ML models prioritizing general training samples over extreme temperature events[63]. Moreover, it is essential to emphasize that regions with lower station density may significantly impact the model's performance. The spatial variability of estimation errors is primarily due to differences in terrain and the uneven distribution of meteorological stations. Although the model accounts for elevation factors, the challenging terrain and lower station density in remote and mountainous areas can reduce accuracy compared to the eastern plains. Limited station density may not adequately capture temperature variations due to terrain fluctuations, leading to higher estimation errors. This effect is more pronounced when estimating daily T_{max} and T_{min} than T_{mean}, due to the temporal discontinuity of extreme temperature values and their susceptibility to terrain influence. Therefore, future research must comprehensively acknowledge the distinct influences of factors such as complex terrain, landscape heterogeneity, and meteorological station density. Developing temperature inversion strategies tailored for mountainous and sparse regions with fewer stations is imperative.

Moreover, temporal variability in RMSE, with lower errors in summer and higher in winter, is primarily due to more minor temperature variations between stations in summer[13] and reduced LST accuracy in cold, dry winter conditions[64]. The error pattern, where T_{max} has lower RMSE than T_{min} in winter and the reverse in summer, is influenced by the temporal lag between Ta and LST, and the stronger correlation between summer T_{min} and LST[65]. Although the estimation models have accounted for the influences of daily and monthly cycles in Ta parameters, this may still be insufficient to counteract the effects of seasonal changes fully. Therefore, in further research, it is advisable to consider separate monthly modelling to enhance the precision of the models.

Code availability

Codes for data and result analysis are freely available at https://zenodo.org/records/11908106[66].

Received: 19 June 2024; Accepted: 7 October 2024;
Published online: 15 October 2024

References

1. Chadburn, S. E. *et al*. An observation-based constraint on permafrost loss as a function of global warming. *Nat. Clim. Change* **7**, 340–344 (2017).
2. Hadi Ahmad, M. *et al*. Modeling the influence of daily temperature and precipitation extreme indices on vegetation dynamics in Katsina State using statistical downscaling model (SDM). *Ecol. Indic.* **155**, 110979 (2023).
3. Zhang, K. *et al*. Increased heat risk in wet climate induced by urban humid heat. *Nature* **617**, 738–742 (2023).
4. Shen, C., Zhu, W. & Xu, L. Critical risk determination method of energy-flow network for urban electricity system under extreme heat wave impact. *Environ. Res.* **191**, 110143 (2020).
5. Ma, W. *et al*. The short-term effect of heat waves on mortality and its modifiers in China: An analysis from 66 communities. *Environ. Int.* **75**, 103–109 (2015).
6. Sun, X. *et al*. Heat wave impact on mortality in Pudong New Area, China in 2013. *Science of The Total Environment* **493**, 789–794 (2014).
7. Weiss, D. J. *et al*. Air temperature suitability for Plasmodium falciparum malaria transmission in Africa 2000–2012: a high-resolution spatiotemporal prediction. *Malar. J.* **13**, 171 (2014).
8. Chen, J. *et al*. Cold spell and mortality in 31 Chinese capital cities: Definitions, vulnerability and implications. *Environ. Int.* **128**, 271–278 (2019).
9. Ding, T. & Qian, W. Geographical patterns and temporal variations of regional dry and wet heatwave events in China during 1960–2008. *Adv. Atmos. Sci.* **28**, 322–337 (2011).
10. Chen, F., Liu, Y., Liu, Q. & Qin, F. A statistical method based on remote sensing for the estimation of air temperature in China: An Estimation Method of Air Temperature Based on Remote Sensing. *Int. J. Climatol.* **35**, 2131–2143 (2015).
11. Hooker, J., Duveiller, G. & Cescatti, A. A global dataset of air temperature derived from satellite remote sensing and weather stations. *Sci. Data* **5**, 180246 (2018).
12. Funk, C. *et al*. A High-Resolution 1983–2016 Tmax Climate Data Record Based on Infrared Temperatures and Stations by the Climate Hazard Center. *J. Climate* **32**, 5639–5658 (2019).
13. Yao, R. *et al*. Global seamless and high-resolution temperature dataset (GSHTD), 2001–2020. *Remote Sens. Environ.* **286**, 113422 (2023).
14. Fang, S. *et al*. Dataset of daily near-surface air temperature in China from 1979 to 2018. *Earth Syst. Sci. Data* **14**, 1413–1432 (2022).
15. Wang, P. *et al*. A daily highest air temperature estimation method and spatial–temporal changes analysis of high temperature in China from 1979 to 2018. *Geosci. Model Dev.* **15**, 6059–6083 (2022).
16. Kilibarda, M. *et al*. Spatio-temporal interpolation of daily temperatures for global land areas at 1 km resolution. *Journal of Geophysical Research: Atmospheres* **119**, 2294–2313 (2014).
17. Zhang, T., Zhou, Y., Wang, L., Zhao, K. & Zhu, Z. Estimating 1 km gridded daily air temperature using a spatially varying coefficient model with sign preservation. *Remote Sens. Environ.* **277**, 113072 (2022).
18. Chen, Y. *et al*. An all-sky 1 km daily land surface air temperature product over mainland China for 2003–2019 from MODIS and ancillary data. *Earth Syst. Sci. Data* **13**, 4241–4261 (2021).
19. Zhang, T. *et al*. A global dataset of daily maximum and minimum near-surface air temperature at 1 km resolution over land (2003–2020). *Earth Syst. Sci. Data* **14**, 5637–5649 (2022).
20. Zhu, W., Lű, A. & Jia, S. Estimation of daily maximum and minimum air temperature using MODIS land surface temperature products. *Remote Sens. Environ.* **130**, 62–73 (2013).
21. Hou, P. *et al*. Near-surface air temperature retrieval from satellite images and influence by wetlands in urban region. *Theor. Appl. Climatol.* **111**, 109–118 (2013).
22. Wang, Y., Liu, J. & Zhu, W. Estimation of Instantaneous Air Temperature under All-Weather Conditions Based on MODIS Products in North and Southwest China. *Remote Sensing* **15**, 2701 (2023).
23. Zhu, W., Lű, A., Jia, S., Yan, J. & Mahmood, R. Retrievals of all-weather daytime air temperature from MODIS products. *Remote Sens. Environ.* **189**, 152–163 (2017).
24. Wang, M. *et al*. Comparison of Spatial Interpolation and Regression Analysis Models for an Estimation of Monthly Near Surface Air Temperature in China. *Remote Sensing* **9**, 1278 (2017).
25. Zhang, Z. & Du, Q. A Bayesian Kriging Regression Method to Estimate Air Temperature Using Remote Sensing Data. *Remote Sensing* **11**, 767 (2019).
26. Gao, M., Li, Z., Tan, Z., Li, H. & Peng, J. Use of Google Earth Engine to Generate a 20-Year 1 Km × 1 Km Monthly Air Temperature Product Over Yellow River Basin. *IEEE J. Sel. Topics Appl. Earth Observ. Remote Sens.* **14**, 10079–10090 (2021).
27. Tran, D.-P. & Liou, Y.-A. Creating a spatially continuous air temperature dataset for Taiwan using thermal remote-sensing data and machine learning algorithms. *Ecol. Indic.* **158**, 111469 (2024).
28. Noi, P., Degener, J. & Kappas, M. Comparison of Multiple Linear Regression, Cubist Regression, and Random Forest Algorithms to Estimate Daily Air Surface Temperature from Dynamic Combinations of MODIS LST Data. *Remote Sensing* **9**, 398 (2017).
29. Wang, C., Bi, X., Luan, Q. & Li, Z. Estimation of Daily and Instantaneous Near-Surface Air Temperature from MODIS Data Using Machine Learning Methods in the Jingjinji Area of China. *Remote Sensing* **14**, 1916 (2022).
30. Rao, Y. *et al*. Estimating daily average surface air temperature using satellite land surface temperature and top-of-atmosphere radiation products over the Tibetan Plateau. *Remote Sens. Environ.* **234**, 111462 (2019).
31. Yao, R. *et al*. Long-term trends of surface and canopy layer urban heat island intensity in 272 cities in the mainland of China. *Science of The Total Environment* **772**, 145607 (2021).
32. Venter, Z. S., Brousse, O., Esau, I. & Meier, F. Hyperlocal mapping of urban air temperature using remote sensing and crowdsourced weather data. *Remote Sens. Environ.* **242**, 111791 (2020).
33. Zhang, Z. & Du, Q. Hourly mapping of surface air temperature by blending geostationary datasets from the two-satellite system of GOES-R series. *Isprs J. Photogramm. Remote Sens.* **183**, 111–128 (2022).
34. Zhang, Z. & Du, Q. Merging framework for estimating daily surface air temperature by integrating observations from multiple polar-orbiting satellites. *Science of The Total Environment* **812**, 152538 (2022).
35. Zhang, Z., Liang, Y., Zhang, G. & Liang, C. Large-Scale Estimation of Hourly Surface Air Temperature Based on Observations from the FY-4A Geostationary Satellite. *Remote Sensing* **15**, 1753 (2023).
36. Qin, R. *et al*. HRLT: a high-resolution (1 d, 1 km) and long-term (1961–2019) gridded dataset for surface temperature and precipitation across China. *Earth Syst. Sci. Data* **14**, 4793–4810 (2022).
37. Sun, H. *et al*. Spatial Resolved Surface Ozone with Urban and Rural Differentiation during 1990–2019: A Space–Time Bayesian Neural Network Downscaler. *Environ. Sci. Technol.* **56**, 7337–7349 (2022).
38. Wei, J. *et al*. Reconstructing 1-km-resolution high-quality PM2.5 data records from 2000 to 2018 in China: spatiotemporal variations and policy implications. *Remote Sens. Environ.* **252**, 112136 (2021).
39. Wei, J. *et al*. Improved 1 km resolution PM_{2.5} estimates across China using enhanced space–time extremely randomized trees. *Atmos. Chem. Phys.* **20**, 3273–3289 (2020).
40. Wei, J. *et al*. Estimating 1-km-resolution PM2.5 concentrations across China using the space-time random forest approach. *Remote Sens. Environ.* **231**, 111221 (2019).
41. Wei, J. *et al*. Ground-Level NO_2 Surveillance from Space Across China for High Resolution Using Interpretable Spatiotemporally Weighted Artificial Intelligence. *Environ. Sci. Technol.* **56**, 9988–9998 (2022).

42. Wei, J. *et al*. Satellite-Derived 1-km-Resolution PM_1 Concentrations from 2014 to 2018 across China. *Environ. Sci. Technol.* **53**, 13265–13274 (2019).
43. Wei, J. *et al*. Separating Daily 1 km $PM_{2.5}$ Inorganic Chemical Composition in China since 2000 via Deep Learning Integrating Ground, Satellite, and Model Data. *Environ. Sci. Technol*. acs.est.3c00272 https://doi.org/10.1021/acs.est.3c00272 (2023).
44. Li, X., Zhou, Y., Asrar, G. R. & Zhu, Z. Developing a 1 km resolution daily air temperature dataset for urban and surrounding areas in the conterminous United States. *Remote Sensing of Environment* **215**, 74–84 (2018).
45. Yoo, C., Im, J., Park, S. & Quackenbush, L. J. Estimation of daily maximum and minimum air temperatures in urban landscapes using MODIS time series satellite data. *Isprs J. Photogramm. Remote Sens.* **137**, 149–162 (2018).
46. Zeng, L. *et al*. 8-Day and Daily Maximum and Minimum Air Temperature Estimation via Machine Learning Method on a Climate Zone to Global Scale. *Remote Sensing* **13**, 2355 (2021).
47. Zhang, T., Zhou, Y., Zhu, Z., Li, X. & Asrar, G. A global seamless 1 km resolution daily land surface temperature dataset (2003 – 2020). *Iowa State University* https://doi.org/10.25380/iastate.c.5078492.v3 (2021).
48. Zhang, T., Zhou, Y., Zhu, Z., Li, X. & Asrar, G. R. A global seamless 1 km resolution daily land surface temperature dataset (2003–2020). *Earth Syst. Sci. Data* **14**, 651–664 (2022).
49. Utkin, L. V., Meldo, A. A. & Konstantinov, A. V. Deep Forest as a framework for a new class of machine-learning models. *Natl. Sci. Rev.* **6**, 186–187 (2019).
50. Du, B. *et al*. A Novel Fully Coupled Physical–Statistical–Deep Learning Method for Retrieving Near-Surface Air Temperature from Multisource Data. *Remote Sensing* **14**, 5812 (2022).
51. Zhang, H. *et al*. HiMIC-Monthly: A 1 km high-resolution atmospheric moisture index collection over China, 2003–2020. *Sci. Data* **11**, 425 (2024).
52. Wei, J. *et al*. Long-term mortality burden trends attributed to black carbon and PM2·5 from wildfire emissions across the continental USA from 2000 to 2020: A deep learning modelling study. *The Lancet Planetary Health* **7**, e963–e975 (2023).
53. Wei, J. *et al*. First close insight into global daily gapless 1 km PM2.5 pollution, variability, and health impact. *Nat Commun* **14**, 8349 (2023).
54. Wang, M., Wei, J., Wang, X., Luan, Q. & Xu, X. All-sky daily max ambient air temperature datasets at 1-km resolution from 2013–2022 in China. *Zenodo* https://doi.org/10.5281/zenodo.10983207 (2024).
55. Wang, M., Wei, J., Wang, X., Luan, Q. & Xu, X. All-sky daily max ambient air temperature datasets at 1-km resolution from 2003–2012 in China. *Zenodo* https://doi.org/10.5281/zenodo.10983219 (2024).
56. Wang, M., Wei, J., Wang, X., Luan, Q. & Xu, X. All-sky daily min ambient air temperature datasets at 1-km resolution from 2003–2012 in China. *Zenodo* https://doi.org/10.5281/zenodo.10951766 (2024).
57. Wang, M., Wei, J., Wang, X., Luan, Q. & Xu, X. All-sky daily min ambient air temperature datasets at 1-km resolution from 2013–2022 in China. *Zenodo* https://doi.org/10.5281/zenodo.10983199 (2024).
58. Wang, M., Wei, J., Wang, X., Luan, Q. & Xu, X. All-sky daily mean ambient air temperature datasets at 1-km resolution from 2003–2012 in China. *Zenodo* https://doi.org/10.5281/zenodo.10947354 (2024).
59. Wang, M., Wei, J., Wang, X., Luan, Q. & Xu, X. All-sky daily mean ambient air temperature datasets at 1-km resolution from 2013–2022 in China. *Zenodo* https://doi.org/10.5281/zenodo.10983177 (2024).
60. Wang, J. & Yan, Z. Rapid rises in the magnitude and risk of extreme regional heat wave events in China. *Weather Clim. Extremes* **34**, 100379 (2021).
61. Zhang, P., Dai, E., Wu, C., Hu, J. & Liu, F. Viewing China's escalating heatwaves through the lens of complex networks. *Ecol. Indic.* **157**, 111248 (2023).
62. Liu, J., Ren, Y., Tao, H. & Shalamzari, M. J. Spatial and Temporal Variation Characteristics of Heatwaves in Recent Decades over China. *Remote Sensing* **13**, 3824 (2021).
63. Cho, D., Yoo, C., Im, J., Lee, Y. & Lee, J. Improvement of spatial interpolation accuracy of daily maximum air temperature in urban areas using a stacking ensemble technique. *GIScience & Remote Sensing* **57**, 633–649 (2020).
64. Fick, S. E. & Hijmans, R. J. WorldClim 2: new 1-km spatial resolution climate surfaces for global land areas. *Int. J. Climatol.* **37**, 4302–4315 (2017).
65. Yao, R., Wang, L., Huang, X., Cao, Q. & Peng, Y. A method for improving the estimation of extreme air temperature by satellite. *Science of The Total Environment* **837**, 155887 (2022).
66. Wang, M. & Luan, Q. *Code for monitoring and analysing extreme weather events (2003–2022).* https://doi.org/10.5281/zenodo.11908106 (2024).

Acknowledgements

This work was supported by the Fengyun Application Pioneer Project [FY-APP-2021.0408] and FY-3 03 Application System Project [FY-3(03)-AS-12.09]. We also thank the Iowa State University's for the seamless daily LST; the NASA Earth Observing System Data and Information System for the MCD18A1 DSR and MOD13A3 DNVI data; the DEM data; and NOAA National Centers for Environmental Information (NCEI) for NTL data. We also thank the ECMWF for the climate reanalysis data.

Author contributions

Q.L., M.W. and J.W. collected and calculated the dataset; M.W. analysed the results and wrote the manuscript; all other authors reviewed and revised the manuscript. M.W. and J.W. are co-first authors.

Competing interests

The authors declare no competing interests.

Additional information

Supplementary information The online version contains supplementary material available at https://doi.org/10.1038/s41597-024-03980-z.

Correspondence and requests for materials should be addressed to Q.L.